Chapter

Real-Time Monitoring of Ionospheric Irregularities and TEC Perturbations

Giorgio Savastano and Michela Ravanelli

Abstract

The ionosphere is a part of the upper atmosphere that is a threat to GNSS and satellite telecommunication systems. In this chapter, we will dive into the GNSS real-time monitoring of ionospheric irregularities and TEC perturbations, with a focus on the detection of small- and medium-scale traveling ionospheric disturbances (TIDs) for natural hazard applications. We will describe the Variometric Approach for Real-Time Ionosphere Observation (VARION) algorithm, which is capable of estimating TEC variations in real time, and it was used to detect tsunami-induced TIDs. In particular, the analytical and physical implications of applying the VARION algorithm both to GNSS dual-frequency MEO (medium Earth orbit) and GEO (geostationary orbit) satellites will be provided, thus highlighting its relevance for natural hazard early warning systems and real-time monitoring of ionospheric irregularities.

Keywords: VARION algorithm, GNSS, GEO, traveling ionospheric disturbances, tsunami early warning systems, ionospheric irregularities

1. Introduction

As the title of this book suggests, the Earth's atmosphere represents a threat for GNSS and telecommunications satellites. In particular, the charged component of the upper atmosphere, the ionosphere, is responsible for errors in GNSS positioning that can reach values of tens of meters for single-frequency GNSS receivers [1, 2]. These errors have to be corrected or eliminated in order to make GNSS a valuable scientific instrument for geodesy and geodynamics applications.

However, the use of GNSS signals is nowdays not only limited to the estimation of the receiver's position, but it has eventually become a key instrument for ionospheric and tropospheric remote sensing studies and for soil features (GNSS reflectometry) [3]. In particular, GNSS can be used to monitor the ionosphere at different time and space scales. On a global scale, GNSS observations are used to generate global ionosphere maps (GIM) by interpolating in both space and time measurements of TEC from stations distributed around the world [4]. On a regional scale, the same signals can be used to detect fast ionospheric disturbances, such as TIDs with periods of minutes to about 1 h [5] and ionospheric scintillation with periods of seconds [6, 7].

The ionosphere is a very important region of the atmosphere as it carries much valuable information about the Earth's system. In fact, the ionosphere is affected from both ends: (a) from above by space weather, such as geomagnetic storms induced by strong solar events, and (b) from below by events such as extreme terrestrial weather and natural hazards.

In this chapter, we focus on the real-time monitoring of ionospheric irregularities and TEC perturbations through the application of the VARION algorithm. In Section 2, we review the main mechanisms by which numerous near-ground geophysical (e.g., earthquakes, volcano eruptions, tsunamis) and man-made (e.g., rocket launches) events induce variations in electron density in the ionosphere. In Section 3, we describe the VARION algorithm, which is capable of estimating in real- time changes in the ionospheres' TEC using stand-alone GNSS receivers and can be used for real-time ionosphere remote sensing. In Section 4 we present the main results of the application of the VARION method for two case studies: the 2012 Haida Gwaii tsunami event and a Falcon 9 rocket launch. In Section 5 we present our conclusions.

2. Earth's surface and ionosphere coupling mechanisms

Acoustic and gravity waves are the two main mechanisms by which energy produced by geophysical events at the Earth's surface can propagate in the atmosphere [8]. The coupling of these atmospheric waves with the ionospheric electron density [9] produces deviations in TEC from the dominant diurnal variation. Traveling ionospheric disturbances (TIDs) are the ionospheric manifestation of these AGWs' induced TEC perturbations. In several applications, such as TID detection, the deviations (also known as fluctuations or perturbations) from the background level are of interest [10, 11]. Other mechanisms by which the ionospheric plasma highly deviates from the dominant diurnal variability are the chemical processes responsible for the ionospheric hole induced by rockets. These processes were described as the interactions between water (H_2O) and hydrogen (H_2) molecules in the exhaust plume and electrons in the ionosphere, through dissociative recombination.

2.1 Acoustic waves

Pressure-induced TEC anomalies from earthquakes were widely observed in the last decade, for example, coseismic ionospheric disturbances (CIDs) were documented with the 2003 M_W 8.3 Tokachi-Oki, Japan and the 2008 M_W 8.1 Wenchuan, China earthquakes [12] observed at Japanese GEONET sites. CIDs produced by the 2011 M_W 9.0 Tohoku-Oki, Japan earthquake were reported by several independent research groups [13, 14]. Volcanic eruptions can also excite acoustic waves and induce anomalies in the TEC measurements [15].

When an earthquake occurs, shock acoustic waves (SAWs) are produced in the proximity of the epicenter (within 500 km), and secondary acoustic waves are caused by surface Rayleigh waves propagating far from the epicenter. These pressure waves, upon reaching the ionosphere, will locally affect electron density through particle collisions between the neutral atmosphere and the ionospheric plasma [16]. SAWs, governed primarily by longitudinal compression, can propagate through the atmosphere at the sound speed which varies from several hundred m/s near sea level to 1 km/s at 400 km altitude [17]. At the height of the ionosphere F layer, it is about 800–1000 m/s [18], so it takes between 10 and 15 min to reach the ionosphere and cause the abovementioned disturbance (CID) [19]. Their waveform

is "N-type wave," consisting of leading and trailing shocks connected by smooth linear transition regions. The waveform arises from nonlinear propagation effects: the amplitude of N waves depends on earthquake magnitude, losses of shock fronts, neutral wind speed, etc. This means that also CID is N-shaped and propagates at such velocity [18]. Rayleigh waves travel along the Earth surface at a velocity of 3–4 km/s. They propagate in the form of a train consisting of several oscillations whose typical period is about ten of seconds [20]. As already mentioned, they trigger secondary acoustic waves emitted in the form of the same train, propagating at sound speed. These waves also appear as CID 10–15 min after the earthquake.

It is important to highlight that only acoustic waves which have a frequency greater than the cutoff frequency can propagate up to the ionosphere [21]. Such frequency is defined as $\omega_a = \frac{\gamma g}{2c_S}$ where c_S is the speed of sound and γ and g are, respectively, the specific heat ratio (of the atmosphere) and gravitational acceleration [22, 23]. Thus, waves with a frequency greater than the cutoff one can reach the ionosphere; otherwise their amplitude decreases exponentially with altitude [22], and in this case, the waves are named evanescent. The typical values of cutoff frequency fall within the range 2.1–3.3 mHz [15, 22].

2.2 Gravity waves

Gravity waves (GW) form when air parcels are lifted due to particular fluid dynamic and then pulled down by buoyancy in an oscillating manner. This can occur when air passes over mountain chains [24] or when a "mountain," which is read as tsunami wave, moves with a certain velocity. Let us imagine the displacement of a volume of atmospheric air from its equilibrium position; it will then find itself surrounded by air with different density. Buoyant forces will try to bring the volume of air back to the undisturbed position, but these restoring forces will overshoot the target and lead it to oscillate about its neutral buoyancy altitude. It will continue this oscillation about an equilibrium point, generating a gravity wave that can propagate up through the ionosphere.

Perturbations at the surface that have periods longer than the time needed for the atmosphere to respond under the restoring force of buoyancy will successfully propagate upward. This is known as the Brunt-Vaisala frequency N and represents the maximum frequency for vertically propagating gravity waves. $N = \sqrt{(g/\theta)(d\theta/dz)}$ where g is the gravitational acceleration, θ is the potential temperature (the temperature that a parcel of air would attain if adiabatically brought to the ground), and z is the altitude.

Tsunamis have periods longer than this frequency and thus excite atmospheric gravity waves (AGWs) that can propagate upward in the atmosphere and ultimately cause perturbations in the ionospheric electron density. As the kinetic energy is conserved up to an altitude of about 200 km, and air density decreases exponentially with altitude, the AGWs are then strongly amplified in the atmosphere. The ratio of the amplitude of the velocity wave between the ionospheric height and the ground level is about 10^4–10^5 [25]. This fact was first established in Daniels [26] and was theoretically further developed in Hines [27, 28]. Therefore, it is possible to remotely detect the effects of ocean tsunamis by observing perturbations in the ionosphere. In detail, AGWs which have frequency lower than the Brunt-Vaisala frequency can propagate up through the ionosphere [22]. In the Earth's atmosphere, it depends on the altitude, and it varies from 3.3 to 1.1 mHz (typical value is 2.9 mHz [22]), corresponding to a buoyancy period of 5 min at sea level and about 15 min at 400 km altitude, near the F region peak of the ionosphere [19].

TIDs can be detected using different observing methods, including ionosondes [29]; ground-based GPS total electron content (TEC) [17, 30]; dual-frequency, space-based altimeters [31]; incoherent backscatter radar (ISR) [32]; and space-based GNSS-RO measurements [33]. Perturbations in the neutral atmosphere after the 2011 Tohoku-Oki tsunami event have also been detected using accelerometers and thruster data from the GOCE mission [34]. Several other causes are responsible for TIDs, such as intense or large-scale tropospheric weather [35], geomagnetic and auroral activity [36, 37], and earthquakes [38–40]. For this reason, the relationship between detected TIDs and those that are induced by a tsunami has to be proven, for example, by verifying that the horizontal speed, direction, and spectral bandwidth of the TIDs match that of the ocean tsunami [5].

The vertical propagation speed of an atmospheric gravity wave at these periods is 40–50 *m/s* [41], so these perturbations should first be observed about 2 *h* after the onset of the tsunami. The TEC anomalies can be identified by their horizontal propagation speed, which is much slower (200–300 *m/s*) than that of the acoustic TID or Rayleigh-wave-induced anomalies and follows the propagation speed of the tsunami itself, which is, much like the Rayleigh waves in the acoustic case, a moving source of gravity waves. However, following the 2011 M_W 9.0 Tohoku-Oki, Japan event, which provided dense near-field TEC observations, it was noted that the onset of the gravity-wave-induced TEC anomalies was shorter, at about 30 *min* after the start of the earthquake, and not the 1.5–2 *h* predicted by previous theoretical computations [17]. This is explained as evidence that it might not be necessary for the gravity wave to reach the F layer peak (around 300 km altitude) for the TEC disturbance to be measurable. Rather, disturbances at lower altitudes within the E layer and the lower portion of the F layer might be substantial enough to be seen in the TEC observations. This is supported by previous modeling results that showed significant TEC perturbations over a broad area around the F layer peak [14]. Through comparisons with tsunami simulations of the event, it was convincingly demonstrated that the tsunami itself must be the source of the observed gravity waves [17]. In light of these observations, ionospheric soundings may be used to monitor tsunamis and issue warnings in advance of their arrival at the coast [3, 5].

2.3 Traveling ionospheric disturbances

Disturbances in the ionosphere naturally occur at many different scales. On a planetary scale, Rossby waves result from latitudinal variations in the strength of the Coriolis effect and have wavelengths of 1000s of km, while, at smaller scales, acoustic gravity waves induced by natural hazards have typical wavelengths in the range of 10-300 km. Based on their phase velocity, wave period, and horizontal wavelength, TIDs are often classified into medium-scale TID (MSTID) and large-scale TID (LSTID). Some guidelines on the properties of these two groups are summarized in **Table 1**, which was created from [42, 43].

In this chapter, we mainly take into account MSTIDs, as they are the one typically generated by tsunami waves and other natural hazards.

	Period [min]	Phase velocity [m/s]	Horizontal wavelength [km]
Large scale	30–300	400–1000	1000–3000
Medium scale	10–60	50–300	10–500

Table 1.
TID classification based on phase velocity, wave period, and horizontal wavelength.

2.4 Dissociative recombination

Several studies were carried out to analyze the ionospheric responses to rocket launches. The first detection of a localized reduction of ionization due to the interaction between the ionosphere and the exhaust plume of the Vanguard II rocket was reported in [44]. More than a decade after that observation, a sudden decrease in total electron content (TEC) was observed after the 1973 NASA's Skylab launch [45] by measuring the Faraday rotation of radio signals from a geostationary satellite. This study [45] was reported a dramatic bite-out of more than 50% of the TEC magnitude having a duration of nearly 4 h and spatial extent of about 1000 km radius. The chemical processes responsible for the ionospheric hole were described as the interactions between water (H_2O) and hydrogen (H_2) molecules in the exhaust plume and electrons in the ionosphere, through dissociative recombination. At the level of concentration at which the reactants (H_2O and H_2) were added to the ionosphere by the rocket's engines, the loss process became 100 times more efficient than the normal loss mechanism in the ionosphere (e.g., N_2). Localized plasma density depletions during rocket launches were detected also using other measurement techniques, such as ground-based incoherent scatter radar and digisonde [46, 47] and continuous Global Positioning System (GPS) receivers [48, 49].

3. VARION approach

Multiple algorithms were developed to estimate useful ionospheric parameters from GNSS signals, such as absolute TEC measurements [4, 50], relative TEC [51, 52], and TEC variations [5]. In this section, we review the main concepts of the VARION approach, which was first presented in [5] for GNSS satellites (Section 3.1) and subsequently expanded to geostationary satellites in [53] (Section 3.2).

3.1 VARION-GNSS

The VARION approach is based on single time differences of geometry-free combinations of GNSS carrier-phase measurements ($L_1 - L_2$), using a stand-alone GNSS receiver and standard GNSS broadcast orbits available in real time. The unknown carrier-phase ambiguity can be considered constant between two consecutive epochs as long as no cycle slips occur. In the case that a cycle slip does occur, then the phase jump can be removed in real time as it represents an outlier in the time series analysis. The receiver and the satellite IFBs in the carrier-phase ionospheric observable are also assumed as constant for a given period [54]. Multipath terms cannot be considered constant between epochs for sampling rates greater than 1 second [55]. However, these terms can be mitigated by applying an elevation cutoff mask of 20 degrees or higher and will be ignored in the following equations for the sake of simplicity. For these reasons, we can write the geometry-free time single-difference observation equation [5], with no need of estimate in real time the phase ambiguity and the IFB:

$$L_{GF}(t+1) - L_{GF}(t) = \frac{f_1^2 - f_2^2}{f_2^2}\left[I_{1R}{}^{S}(t+1) - I_{1R}{}^{S}(t)\right] \tag{1}$$

where the term L_{GF} refers to the geometry-free combination and f_1 and f_2 are the two frequencies in L-band transmitted by any GNSS satellites. Taking into

account the ionospheric refraction along the geometric range, we compute the sTEC variations between two consecutive epochs:

$$\delta sTEC(t+1,t) = \frac{f_1^{\,2} f_2^{\,2}}{A\left(f_1^{\,2} - f_2^{\,2}\right)} \left[L_{GF}(t+1) - L_{GF}(t)\right] \tag{2}$$

where $A = 40.3 \cdot 10^{16}\ [m][Hz]^2[TECU]^{-1}$ is the standard conversion factor linking TEC [TECU] to ionospheric delay in metric unit [meters]. The discrete derivative of *sTEC* over time can be simply computed dividing *δsTEC* by the interval between epochs t and $(t + 1)$. *sTEC* is an integrated quantity representing the total number of electrons included in a column with a cross-sectional area of $1\,m^2$, counted along the signal path s between the satellite S and the receiver R. The sTEC observations are modeled by collapsing them to the ionospheric pierce point (IPP) between the satellite-receiver line-of-sight and the single-shell layer located above the height of F2 peak, where the electron density is assumed to be maximum. The IPP position can be computed in real time using standard GNSS broadcast orbit parameters [5], after having chosen the height of the F2 peak.

In this work, single-shell ionospheric layer approximation was applied to explain the physical meaning of the *δsTEC* values provided by VARION and to explicitly show the effect of the IPP motion in the VARION observation equation. This single-shell ionospheric approximation means that the ionospheric sTEC is assigned to an IPP point which renders a 2D picture without vertical dependence of any parameter. In this 2D representation of the ionosphere, the variation *δsTEC* in the interval δt is equivalent to a total derivative over time where the observational point (IPP) moves independently of the motion of the medium (ionospheric plasma). The total derivative encompasses both the variation in time in a certain fixed position (sTEC partial time derivative) and the variation in time due to the sTEC horizontal spatial variation and to the horizontal motion of the IPP relative to the horizontal plasma flow (the relative IPP velocity times the sTEC 2D space gradient on the ionospheric layer); therefore the VARION-MEO (hereafter called VARION-GNSS):

$$\frac{d\,sTEC(t,s)}{dt} = \frac{\partial\,sTEC(t,s)}{\partial t} + \left(\vec{V}_{pla} - \vec{V}_{ipp}\right) \cdot \nabla sTEC(t,s), \tag{3}$$

where $\vec{V}_{pla}$ and $\vec{V}_{ipp}$ are the horizontal plasma and IPP vector velocity field in an Earth-centered Earth-fixed (ECEF) reference frame (WGS84, in our case, since we are using broadcast orbits), respectively, and $\nabla sTEC(t,s)$ is the horizontal spatial gradient of sTEC. It is clear that the convective derivative term accounts for IPP motion and plasma motion $(\vec{V}_{pla} - \vec{V}_{ipp})$. It is important to underline that in a full 3D representation of the ionosphere, $\vec{V}_{pla}$, $\vec{V}_{ipp}$, and $\nabla sTEC(t,s)$ are altitude-dependent terms; in our 2D single-shell ionospheric layer approximation, all these terms are referred to a 300 km height. However, for the purpose of this paper, Eq. (3) already shows that the ionospheric remote sensing based on GNSS observations acquired from MEO satellites depends on the time-dependent position of the IPPs. It is crucial to underline that the $\vec{V}_{ipp}$ magnitude is not constant during the period of observation, but it increases for lower elevation angles [56]. In [53] it was shown that the $\vec{V}_{ipp}$ magnitudes range 40–120 m/s for elevation angles 30–90 degrees, meaning that these IPPs have a velocity of the same order of magnitude of most of the ionospheric perturbations induced by natural hazards (e.g., tsunami-induced TIDs). Also, the background noise, and long period trends of *δsTEC* in

Eq. (3), increases for lower elevation angles, when the length of the signal path inside the ionosphere is longer, leading to larger *δsTEC* values. This explains the current limitation of GNSS ionospheric-based early warning algorithms for low elevation angles. In particular, it is a common practice to apply a cutoff elevation angle for GNSS ionospheric remote sensing studies which is much higher (20 degrees or higher) than the one normally used for GNSS positioning applications (5 degrees or lower).

After identifying and removing cycle slips from *δsTEC* time series, we integrate Eq. (3) over time in order to reconstruct the final Δ*sTEC* perturbation term. The VARION approach overcomes the problem of estimating the phase initial ambiguity and the satellite inter-frequency biases (IFBs), which can be assumed constant for a given period [5], thus being ideal for real-time applications.

3.2 VARION-geo

A GEO satellite experiences libration only (i.e., drifting back and forth between two stable points), so that it can be considered motionless relative to an ECEF reference frame, and as a result the IPP's velocity vector $\vec{V}_{ipp}$ is negligible. For this reason, Eq. (3) becomes:

$$\frac{d\,sTEC(t,s)}{dt} = \frac{\partial\,sTEC(t,s)}{\partial t} + \vec{V}_{pla} \cdot \nabla sTEC(t,s), \tag{4}$$

which can be considered the new VARION-GEO observable. Eq. (4) formally reveals the fundamental property of GEO satellites: independence of the estimated *δsTEC* value on the motion of the IPP. Since GEO observations have a constant elevation angle, we can assume a constant level of observational noise throughout the entire period of observation. Furthermore, GEO observations are less prone to trends induced at low elevation angles, when the length of the signal path inside the ionosphere is longer, leading to larger *δsTEC* values. The other important advantage of GEO satellites is the fact that they provide long-term continuous time series over a fixed location.

4. Main results

In this section, we will give an outlook on the main results achieved through the VARION approach. In particular, we will show the main results from [5] for tsunami-generated TID detection (Section 4.1) and from [53] for ionospheric plasma depletion analysis (Section 4.2). For more details on these test cases and on the related data processing performed with VARION, please refer to the cited papers.

4.1 Haida Gwaii tsunami-induced TIDs

4.1.1 Dataset

Using the VARION algorithm, we compute TEC variations induced by the 2012 Haida Gwaii tsunami event at 56 GPS receivers from Plate Boundary Observatory (PBO) in Hawaiian Islands. All the GPS permanent stations are located in Big Island (see **Figure 1**) and acquired observations at 15 and 30 second rate. In order to validate the methodology, results were, hence, compared with the real-time

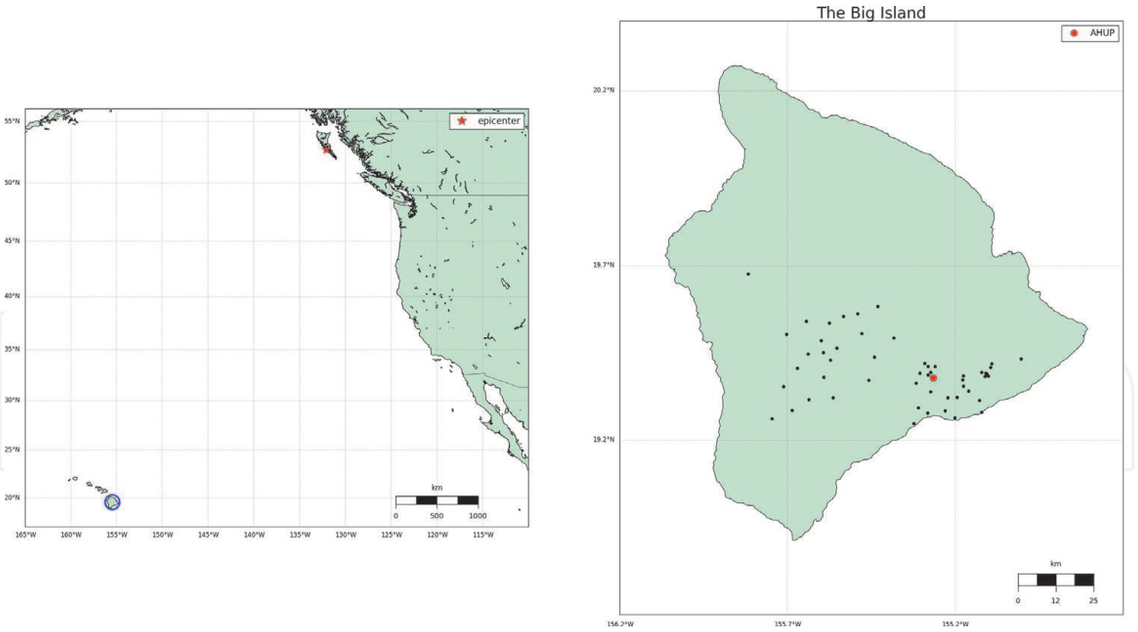

Figure 1.
Map indicating the epicenter of the 10/27/2012 Canadian earthquake (left panel) and zoomed-in image of the Hawaii big island, where the 56 used GPS stations are located. Figure adapted from Savastano et al. [5].

tsunami Method of Splitting Tsunami (MOST) model produced by the NOAA Center for Tsunami Research [57, 58].

4.1.2 Results and discussion

VARION processing outcame a TEC perturbation with amplitudes of up to 0.25 TEC units and traveling ionospheric perturbations (TIDs) moving away from the earthquake epicenter at an approximate speed of 277 *m/s*. To better study the localized variations of power in the TEC time series, a Paul wavelet analysis was performed [59, 60]. We find perturbation periods consistent with a tsunami typical deep ocean period. In particular, periods in the range of 10–30 min were obtained: these periods are similar to the ones of the tsunami ocean waves, which can range from 5 min up to an hour with the typical deep ocean period of only 10–30 wavelengths around 400 km and the velocity approximately 200 m/s.

Figure 2 shows the sTEC time series wavelet analysis for the seven satellites in view at the station AHUP. The upper panels show the sTEC time series obtained with the VARION software in a real-time scenario. The bottom panels indicate the wavelet spectra. The colors represent the intensity of the power spectrum, and the black contour encloses regions of greater than 95% of confidence for a red noise process. We can identify five satellites (PRNs 4, 7, 8, 10, 20) with peaks consistent in time and period with the tsunami ocean waves. These results clearly show TIDs appearing after the tsunami reached the islands, with an increase of the power spectrum for periods between 10 and 30 min during the TIDs.

Figure 3 shows time sTEC variations for 2 h (08:00–10:00 UT – 28 October 2012) at the IPPs vs. distance from the Haida Gwaii earthquake epicenter, for the same seven satellites under consideration. The TIDs are clearly visible in the interval of significant sTEC variations (from positive to negative values and vice versa). The vertical and horizontal black lines represent the time (when the tsunami arrived at the Hawaii Islands) and the distance (between the epicenter and the Big Island), respectively. In this way, we identify the green rectangle as the alert area, and it is evident that satellite PRN 10, the closest to the earthquake epicenter, detected TIDs before the tsunami arrived at Hawaiian Islands (08:30:08 UT). In the

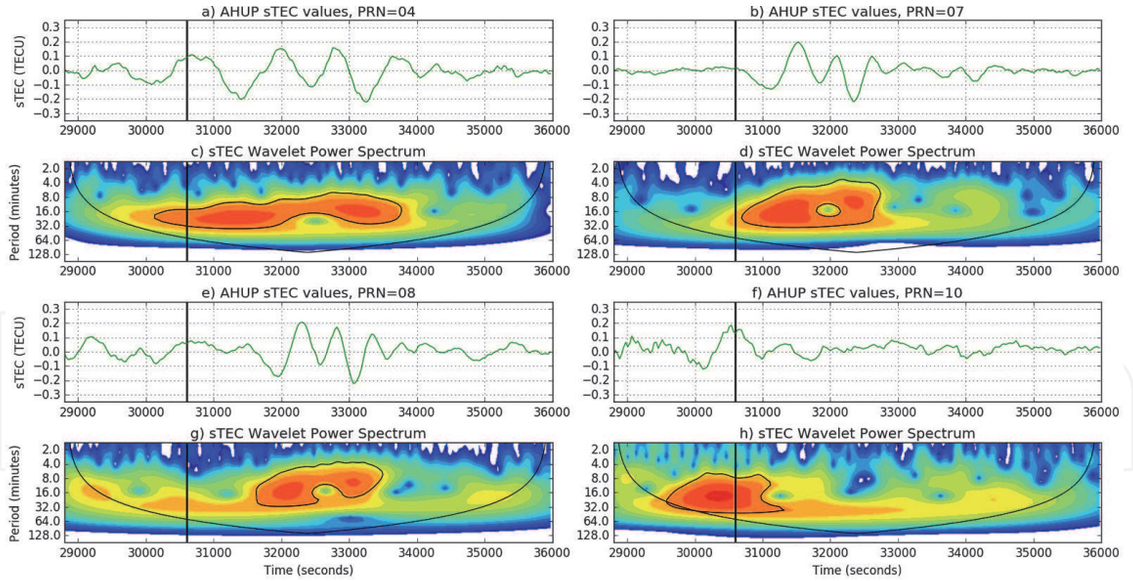

Figure 2.
(a), (b), (e), (f) Four of 260 time series used for the wavelet analysis, station AHUP, satellite PRN 4, 7, 8, 10. (c), (d), (g), (h) the wavelet power spectrum used the Paul wavelet. The vertical axis displays the Fourier period (min), while the horizontal axis is time (s). The black vertical line represents the time when the tsunami reached the Hawaiian islands. The color panels represent the intensity of the power spectrum; the black contour encloses regions of greater than 95% confidence for a red noise process with a lag-1 coefficient of 0.72; the external black line indicates the cone of influence, the limit outside of which edge effects may become significant. Figure adapted from Savastano et al. [5].

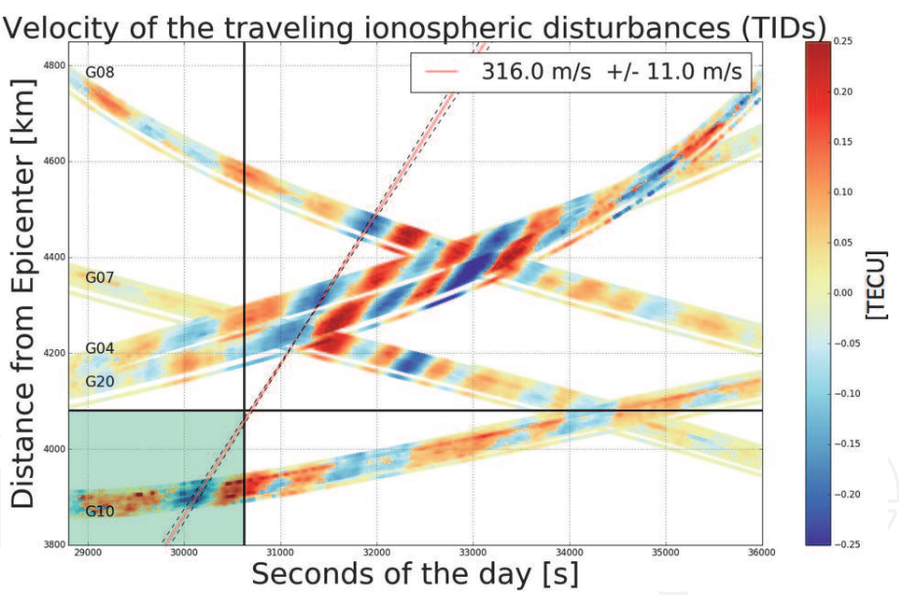

Figure 3.
sTEC variations for 2 h (08:00–10:00 UT – 28 October 2012) at the IPPs vs. distance from the Haida Gwaii earthquake epicenter, for the 7 satellites observed from the 56 Hawaii big islands GPS permanent stations. The TIDs are clearly visible in the interval of significant sTEC variations (from positive to negative values and vice versa). The vertical and horizontal black lines represent the time (when the tsunami arrived at the Hawaii Islands) and the distance (between the epicenter and the big island), respectively; it is evident that PRN 10 detected TIDs before the tsunami arrived at Hawaii Islands (08:30:08 UT). The slope of the straight line fitted, considering a linear least squares regression for corresponding sTEC minima for different satellites, represents the TIDs' mean propagation velocity. Figure adapted from Savastano et al. [5].

distance vs. time plots (also called hodochrons), the slope of the straight line, fitted considering corresponding sTEC minima for different satellites, represents the horizontal speed estimate of TIDs. This plot indicates that the linear least squares' estimated speed of the TIDs is about 316 m/s, and it is found to be in good

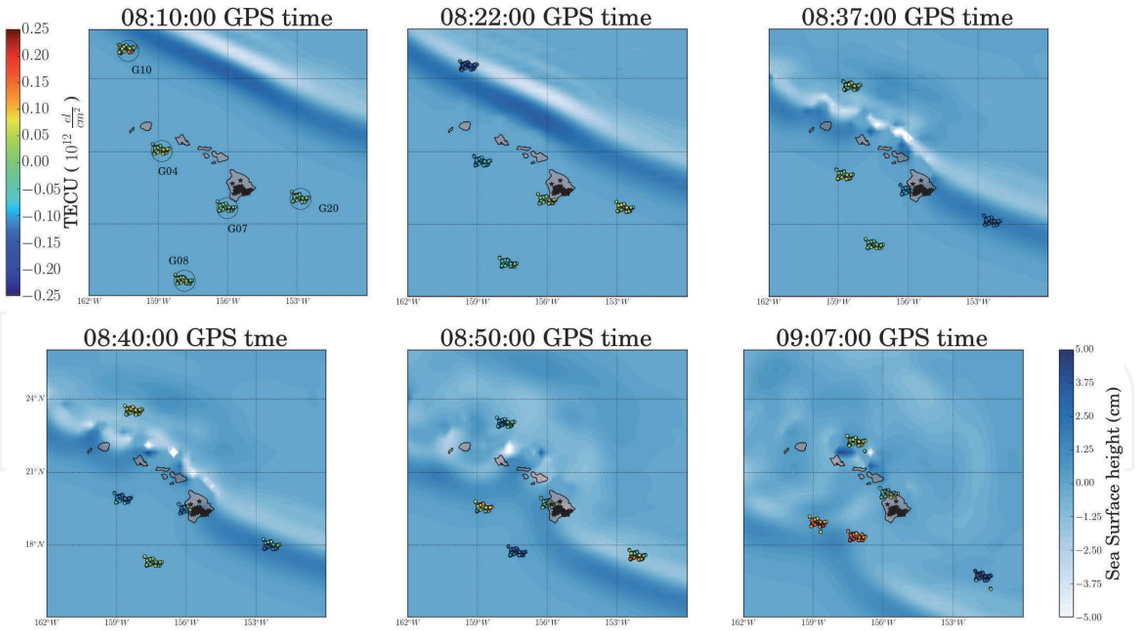

Figure 4.
Space–time sTEC variations at six epochs within the 2-h interval (08:00–10:00 UT – 28 October 2012) at the SIPs for the five satellites showing TIDs over-plotted the tsunami MOST model. TIDs are consistent in time and space with the tsunami waves. Figure adapted from Savastano et al. [5].

agreement with a typical speed of the tsunami gravity waves estimated with ground-based GNSS receivers.

Figure 4 displays a sequence of maps of the region around the Hawaiian Islands showing the variations in sTEC (determinable in real time) at IPP/SPI locations on top of the MOST model sea-surface heights. Note that, just as the MOST model wavefronts are moving past the IPPs, the sTEC variations in the region become pronounced, correlated with the passage of the ocean tsunami itself. In particular, at 08:22:00 GPS time (08:21:44 UT), we are able to see sTEC perturbations from 56 stations looking at satellite PRN 10. The propagation of the MOST modeled tsunami passes the ionospheric pierce points located NW of the Big Island and offers insight with regard to the ionospheric response to the tsunami-driven atmospheric gravity wave. These perturbations are detected before the tsunami reached the islands as seen from the locations of the SIP points. The following frames indicate the tsunami-driven TIDs detected from the other four satellites (PRNs 4, 7, 8, 20) tracking the propagating tsunami (see supplementary video SV1 online).

4.2 Falcon 9 rocket-induced ionospheric plasma depletion

4.2.1 Dataset

To estimate the slant TEC variations associated with the rocket launch, we applied the VARION algorithm to the WAAS-GEO observations collected at 62 Plate Boundary Observatory (PBO) sites located in California (https://www.unavco.org/instrumentation/networks/status/pbohttps://www.unavco.org/instrumentation/networks/status/pbo). In this study, we used satellite S35 (PRN 135) located at 133 degree West and satellite S38 (PRN 138) located at 107.3 degree West. **Figure 5** (left panel) shows the IPP location for satellites S35 (blue dots) and S38 (yellow dots) and the location of the ionosonde site PA836 (red dot). We use the standard single-shell ionospheric layer approximation at the height of 300 km to calculate the IPP locations [61]. On the right, two maps representing the Earth as seen from these

two GEO satellites are shown. The raw GEO observations are available in RINEX format with a sampling rate of 15 seconds.

The ionosonde observations from site PA836 (located less than 5 kilometers from the Vandenberg Air force Base) are used here for an independent comparison with the VARION-GEO solutions. The electron density profiles derived from the sweeping ionosonde observations extend from the lower E region to the F region peak with 15 min of cadence.

4.2.2 Results and discussion

Figure 6(a) shows the closest VARION-GEO Δ*sTEC* time series to the ionosonde site and (b) shows the ionosonde peak electron density (NmF2)

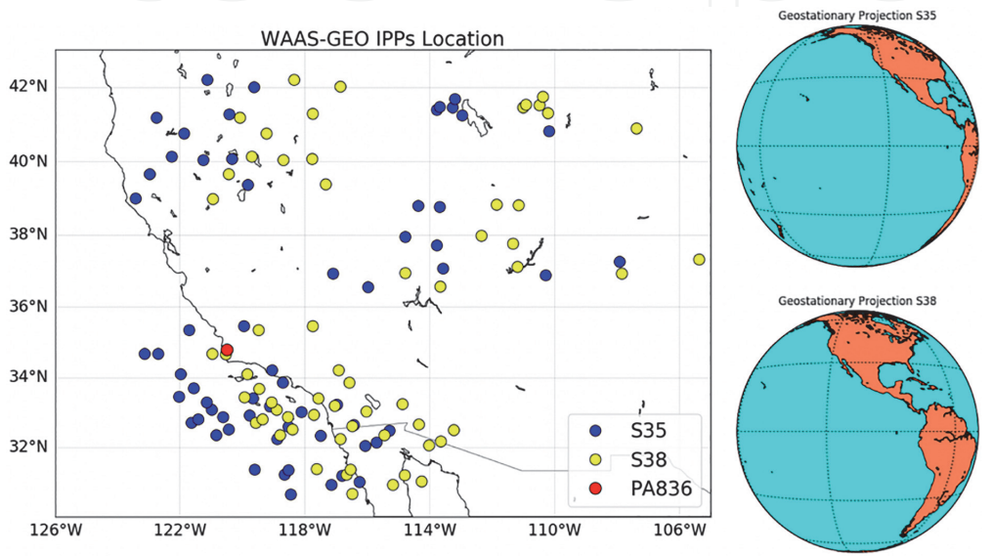

Figure 5.
Map showing the IPP location for satellites S35 (blue dots) and S38 (yellow dots) seen from the 62 GNSS stations. The IPPs for GEO satellites can be considered to be fixed over time. The red dot represents the location of the ionosonde site PA836. On the right, we display two maps representing the earth as seen from WAAS-GEO satellites S35 and S38. Figure adapted from Savastano et al. [53].

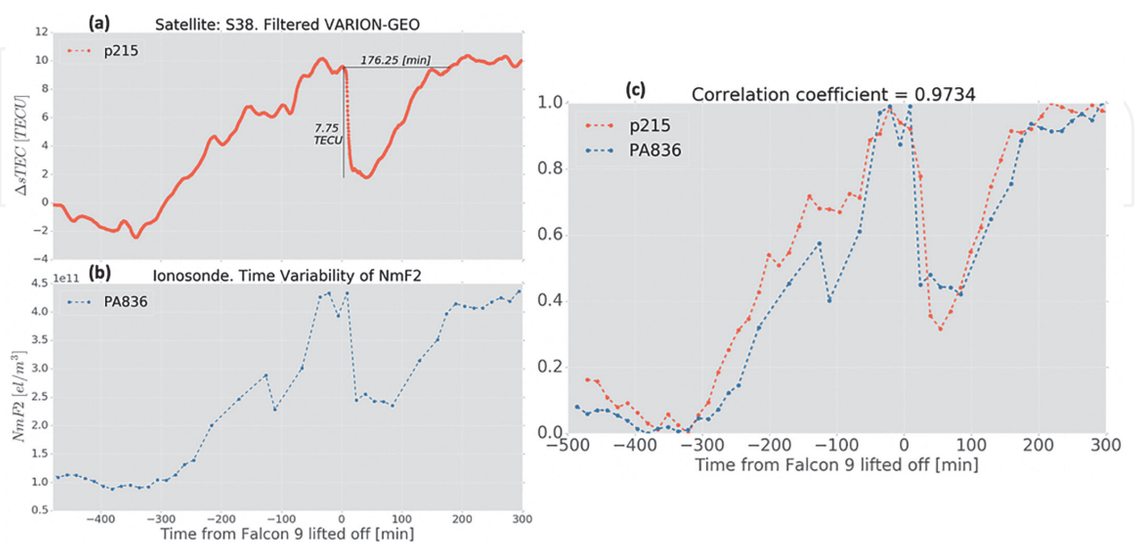

Figure 6.
(a) Shows the VARION-GEO ΔsTEC solutions obtained from station p215, satellite S38. (b) Shows the NmF2 time variability obtained from ionosonde PA836. (c) Shows the down-sampled and normalized ΔsTEC solutions (red curve) and the normalized NmF2 time series (blue curve) plotted using a common scale [0, 1]. This figure shows a high correlation between the VARION-GEO ΔsTEC solutions and ionosonde data. The correlation coefficient between the two curves is 0.97. Figure adapted from Savastano et al. [53].

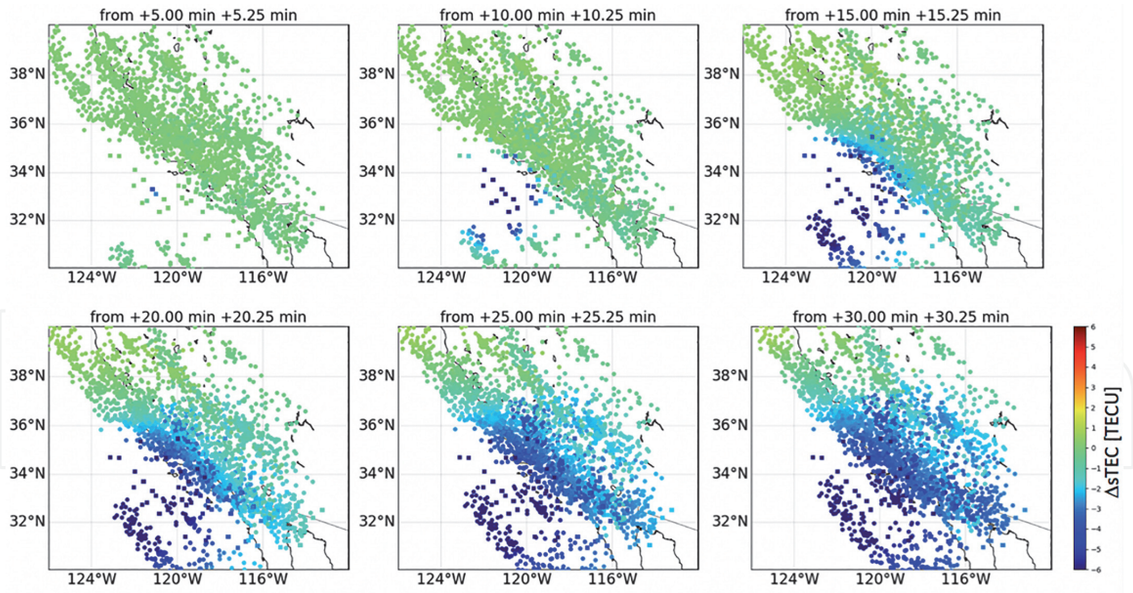

Figure 7.
Space–time ΔsTEC variations for 30 min after the launch (one frame every 5 min) at the SIPs (same positions of the corresponding IPPs on the map) for the 2 GEO satellites (square symbols) and 6 GPS satellites (denoted by circles) seen from the 62 GNSS permanent stations. The ionospheric hole is detected from both GEO satellites 5 min after the rocket launch. The coordinates are expressed in geodetic latitude (in degrees north) and longitude (in degrees west). Figure adapted from Savastano et al. [53].

extracted for each electron density profile measured by the ionosonde and plotted as a function of time. An electron density depletion in the F2 layer is clearly visible from both data sets. In order to quantify the agreement between the two curves, we applied a min-max normalization to the two curves to bring all values into the range [0, 1]. This procedure allows us to study the correlation between the two curves: **Figure 6(c)** displays the normalized Δ*sTEC* (red) and NmF2 (blue) curves. We then down-sampled the normalized VARION-GEO solutions in order to have the same sampling rate as the ionosonde data (15 min). Finally, we computed the correlation coefficient between the two curves, and we found a value of 0.97. Despite the fact the ionosonde electron density profiles extend up to the F2 peak, and that two measurements are not exactly co-located, the agreement between the two datasets is very good.

Figure 7 displays a sequence of six maps (every 5 min) in the region around Vandenberg Air Force Base in California. These maps show the VARION-GEO Δ*sTEC* solutions at GEO-IPP locations for satellites S35 and S38 (squared markers) and the VARION-GPS solutions for satellites G02, G05, G06, G12, G25, and G29 (circle markers). The colors represent variations in the Δ*sTEC*. The ionospheric hole (blue color) is clearly detected from both GEO satellites 5 min after the rocket launch. The GPS satellites start detecting the ionospheric hole as they are moving inside the depleted ionospheric region. This figure well illustrates the difference between GEO and GPS solutions. VARION-GEO solutions provide a direct estimation of the time evolution of the ionosphere over a fixed location, while VARION-GPS solutions are also affected by the ionospheric spatial gradients as they move along the IPP trajectory (Section 3.2). The figure shows the potential benefits of GEO satellites as a complementary technique for well-established GPS satellites.

5. Conclusions

It is widely known that ionospheric anomalies can be a threat to GNSS and satellite telecommunications; therefore real-time monitoring of the ionosphere

represents an important outreach. This chapter finds its reasons in this background, but in the meantime it extends its fields of application to natural hazard early warning systems. It represents an overview about the possible real-time VARION applications for the monitoring of ionospheric irregularities and TEC perturbations.

The VARION is based on single time difference of geometry-free combination of carrier-phase observations that makes it suitable for real-time application. The VARION algorithm was applied both to standard GNSS MEO satellites and to GNSS GEO satellites. It is important to underline that these analyses were carried out in real-time scenario: only data available in real time were used.

In detail, the 2012 Haida Gwaii tsunami event represents a fundamental study case as it showed for the first time that real-time detection of tsunami-induced TEC perturbations is possible and that these TIDs become clear before the tsunami waves hit the Hawaii Big Island [5]. This paper demonstrated that real-time GNSS tracking of TEC perturbations can provide information on tsunami propagation that is consistent with that generated by NOAA's current real-time forecast system [62]. The ability of VARION to detect the TIDs before the tsunami arrival represents a valid contribution for the enhancement of tsunami early warning system.

In [53], it was demonstrated that the extension of the VARION algorithm to GEO satellites enabled a better description of the ionospheric plasma depletion induced by a Falcon 9 rocket. These results are relevant for different GNSS applications, since an ionospheric plasma depletion can potentially lead to a range error of several meters. Lastly, the VARION was implemented in the JPL's Global Differential GPS System (GDGPS) real-time interface that may be accessed at (https://iono2la.gdgps.net/), allowing real-time monitoring of the status of the ionosphere.

Therefore, the VARION extreme versatility makes it suitable for real-time ionospheric monitoring and anomaly detection applications.

Acknowledgements

The authors thank Prof. Mattia Crespi for his great support throughout of the drawing up of this chapter.

Conflict of interest

The authors declare no conflict of interest.

Abbreviations

IPP	ionospheric pierce point
SIP	sub-ionospheric pierce point
VARION	Variometric Approach for Real-Time Ionosphere Observation
TIDs	traveling ionospheric disturbances
CIDs	coseismic ionospheric disturbances
MEO	medium Earth orbit
GEO	geostationary orbit
AGWs	atmospheric gravity waves
SAWs	shock acoustic waves
TEC	total electron content
PBO	Plate Boundary Observatory network
WAAS	Wide Area Augmentation System
MOST	Method of Splitting Tsunami

Author details

Giorgio Savastano[1*†] and Michela Ravanelli[2*†]

1 Spire Global, Inc., Luxembourg

2 Geodesy and Geomatics Division – DICEA, Sapienza University of Rome, Rome, Italy

*Address all correspondence to: giorgio.savastano@spire.com and michela.ravanelli@uniroma1.it

† These authors contributed equally.

References

[1] Afraimovich EL, Astafyeva EI, Demyanov VV, Edemskiy IK, Gavrilyuk NS, Ishin AB, et al. A review of GPS/GLONASS studies of the ionospheric response to natural and anthropogenic processes and phenomena. Journal of Space Weather and Space Climate. 2013;**3**:A27

[2] Su K, Jin S, Hoque MM. Evaluation of ionospheric delay effects on multi-gnss positioning performance. Remote Sensing. 2019;**11**(2):171

[3] Larson KM. Unanticipated uses of the global positioning system. Annual Review of Earth and Planetary Sciences. 2019;**47**(1):19-40

[4] Mannucci AJ et al. A global mapping technique for GPS derived ionospheric total electron content measurements. Radio Science. 1998;**33**: 565-582

[5] Savastano G, Komjathy A, Verkhoglyadova O, Mazzoni A, Crespi M, Wei Y, et al. Real-time detection of tsunami ionospheric disturbances with a stand-alone gnss receiver: A preliminary feasibility demonstration. Scientific Reports. 2017;**7**. Article number: 46607

[6] Liu Z, Yang Z, Chen W. A study on ionospheric irregularities and associated scintillations using multi-constellation gnss observations. In: Proc. of ION PNT, Institute of Navigation, Honolulu, Hawaii, USA. 2017

[7] Kintner PM, Ledvina BM, De Paula ER. GPS and ionospheric scintillations. Space Weather. 2007;**5** (9). Article number: S09003

[8] Masashi Hayakawa and Oleg A Molchanov. Seismo Electromagnetics: Lithosphere-Atmosphere-Ionosphere Coupling. 2002

[9] Occhipinti G, Kherani EA, Lognonné P. Geomagnetic dependence of ionospheric disturbances induced by tsunamigenic internal gravity waves. Geophysical Journal International. 2008; **73**:753765

[10] Afraimovich EL, Boitman ON, Zhovty EI, Kalikhman AD, Pirog TG. Dynamics and anisotropy of traveling ionospheric disturbances as deduced from transionospheric sounding data. Radio Science. 1999;**34**(2):477-487

[11] Afraimovich E. The spatio-temporal characteristics of the wave structure excited by the solar terminator as deduced from TEC measurements at the global GPS network. In: EGU General Assembly Conference Abstracts. Vol. 11. 2009. p. 62

[12] Rolland LM, Lognonné P, Munekane H. Detection and modeling of Rayleigh wave induced patterns in the ionosphere. Journal of Geophysical Research: Space Physics. 2011;**116**(A5). Article number: A05320

[13] Komjathy A, Galvan DA, Stephens P, Butala MD, Akopian V, Wilson B, et al. Detecting ionospheric tec perturbations caused by natural hazards using a global network of gps receivers: The tohoku case study. Earth, Planets and Space. 2013;**64**(12):24

[14] Rolland LM, Lognonné P, Astafyeva E, Kherani EA, Kobayashi N, Mann M, et al. The resonant response of the ionosphere imaged after the 2011 off the Pacific coast of Tohoku earthquake. Earth, Planets and Space. 2011;**63**(7):62

[15] Dautermann T, Calais E, Lognonné P, Mattioli GS. Lithosphere-atmosphere-ionosphere coupling after the 2003 explosive eruption of the Soufriere hills volcano, Montserrat.

Geophysical Journal International. 2009; **179**(3):1537-1546

[16] Kherani EA, Lognonné P, Kamath N, Crespon F, Garcia R. Response of the ionosphere to the seismic triggered acoustic waves: Electron density and electromagnetic fluctuations. Geophysical Journal International. 2009;**176**:1-13

[17] Galvan DA et al. Ionospheric signatures of Tohoku-Oki tsunami of march 11, 2011: Model comparisons near the epicenter. Radio Science. 2012;**47**: RS4003

[18] Astafyeva E, Heki K, Kiryushkin V, Afraimovich E, Shalimov S. Two-mode long-distance propagation of coseismic ionosphere disturbances. Journal of Geophysical Research: Space Physics. 2009;**114**(A10). Article number: A10307

[19] Galvan DA, Komjathy A, Hickey MP, Mannucci AJ. The 2009 Samoa and 2010 Chile tsunamis as observed in the ionosphere using GPS total electron content. Journal of Geophysical Research. 2011;**116**:A06318

[20] Afraimovich EL, Perevalova NP, Plotnikov AV, Uralov AM. The shock-acoustic waves generated by the earthquakes. Annales de Geophysique. 2001;**19**:395-409

[21] Ducic V, Artru J, Lognonné P. Ionospheric remote sensing of the Denali earthquake Rayleigh surface waves. Geophysical Research Letters. 2003;**30**(18)

[22] Artru J, Farges T, Lognonné P. Acoustic waves generated from seismic surface waves: Propagation properties determined from Doppler sounding observations and normal-mode modelling. Geophysical Journal International. 2004;**158**(3):1067-1077

[23] Tahira M. Acoustic resonance of the atmospheric at 3.7 hz. Journal of the Atmospheric Sciences. 1995;**52**(15): 2670-2674

[24] Queney P. The problem of airflow over mountains. A summary of theoretical studies. Bulletin of the American Meteorological Society. 1948; **29**:16-26

[25] Rakoto V, Lognonné P, Rolland L, Coisson P. Tsunami wave height estimation from GPS-derived Ionospheric data. Journal of Geophysical Research: Space Physics. 2018;**123**(5): 4329-4348

[26] Daniels FB. Acoustic energy generated by ocean waves. Journal of the Acoustical Society of America. 1952; **24**:83

[27] Hines CO. Internal atmospheric gravity waves at ionospheric heights. Canadian Journal of Physics. 1960;**38**: 14411481

[28] Hines CO. Gravity waves in the atmosphere. Nature. 1972;**239**:7378

[29] Peltier WR, Hines CO. On the possible detection of tsunamis by a monitoring of the ionosphere. Journal of Geophysical Research. 1976;**81**(12): 1995-2000

[30] Rolland LM, Occhipinti G, Lognonné P, Loevenbruck A. Ionospheric gravity waves detected offshore Hawaii after tsunamis. Geophysical Research Letters. 2010;**37**: L17101

[31] Occhipinti G, Lognonné P, Kherani EA, Hbert H. Three-dimensional waveform modeling of ionospheric signature induced by the 2004 Sumatra tsunami. Geophysical Research Letters. 2006; **33**(20). Article number: L20104

[32] Lee MC et al. Did tsunami-launched gravity waves trigger ionospheric

turbulence over Arecibo. Journal of Geophysical Research. 2008;**113**:A01302

[33] Coisson P, Lognonné P, Walwer D, Rolland LM. First tsunami gravity wave detection in ionospheric radio occultation data. Earth and Space Science. 2015;**2**:125-113

[34] Garcia RF, Doornbos E, Bruinsma S, Hebert H. Atmospheric gravity waves due to the Tohoku-Oki tsunami observed in the thermosphere by GOCE. Journal of Geophysical Research-Atmospheres. 2014;**119**(8):4498-4506

[35] Kelley MC. In situ ionospheric observations of severe weather-related gravity waves and associated small-scale plasma structure. Journal of Geophysical Research: Space Physics. 1997;**102**(A1): 329-335

[36] Nicolls MJ, Kelley MC, Coster AJ, Gonzalez SA, Makela JJ. Imaging the structure of a large scale tid using isr and tec data. Geophysical Research Letters. 2004;**31**:L09812

[37] Afraimovich EL, Astafyeva EI, Demyanov VV, Gamayunov IF. Mid-latitude amplitude scintillation of gps signals and gps performance slips. Advances in Space Research. 2009; **43**(6):964-972

[38] Calais E, Minster JB. GPS detection of ionospheric perturbations following the January 17, 1994, Northridge earthquake. Geophysical Research Letters. 1995;**22**(9). 1045-1048

[39] Artru J, Lognonné P, Blanc E. Normal modes modelling of postseismic ionospheric oscillations. Geophysical Research Letters. 2001;**28**(4):697-700

[40] Kelley MC, Livingston R, McCready M. Large amplitude thermospheric oscillations induced by an earthquake. Geophysical Research Letters. 1985;**12**:577-580

[41] Artru J, Ducic V, Kanamori H, Lognonné P, Murakami M. Ionospheric detection of gravity waves induced by tsunamis. Geophysical Journal International. 2005;**20**:840-848

[42] Crowley G, Rodrigues FS. Characteristics of traveling ionospheric disturbances observed by the tiddbit sounder. Radio Science. 2012;**47**(4):1-12

[43] Ogawa T, Igarashi K, Aikyo K, Maeno H. NNSS satellite observations of medium-scale traveling Ionospheric disturbances at southern high-latitudes. Journal of Geomagnetism and Geoelectricity. 1987;**39**(12):709-721

[44] Booker HG. A local reduction of f-region ionization due to missile transit. Journal of Geophysical Research. 1961; **66**(4):1073-1079

[45] Mendillo M, Hawkins GS, Klobuchar JA. A sudden vanishing of the ionospheric F region due to the launch of Skylab. Journal of Geophysical Research. 1975;**80**:2217-2225

[46] Bernhardt PA, Huba JD, Kudeki E, Woodman RF, Condori L, Villanueva F. Lifetime of a depression in the plasma density over Jicamarca produced by space shuttle exhaust in the ionosphere. Radio Science. 2001;**36**: 1209-1220

[47] Bernhardt PA et al. Ground and space-based measurement of rocket engine burns in the ionosphere. IEEE Transactions on Plasma Science. 2012; **40**:1267-1286

[48] Mendillo M, Smith S, Coster A, Erickson P, Baumgardner J, Martinis C. Man-made space weather. Space Weather. 2008;**6**:S09001

[49] Ozeki M, Heki K. Ionospheric holes made by ballistic missiles from North Korea detected with a Japanese dense GPS array. Journal of Geophysical

Research: Space Physics. 2010;**115**(A9). Article number: A09314

[50] Komjathy A, Sparks L, Wilson BD, Mannucci AJ. Automated daily processing of more than 1000 ground-based GPS receivers for studying intense ionospheric storms. Radio Science. 2005;**40**:RS6006

[51] Sardon E, Rius A, Zarraoa N. Estimation of the transmitter and receiver differential biases and the ionospheric total electron content from global positioning system observations. Radio Science. 1994;**29**:577-586

[52] Hajj GA, Lee LC, Pi X, Romans LJ, Schreiner WS, Straus PR, et al. COSMIC GPS ionospheric sensing and space weather. Terrestrial, Atmospheric and Oceanic Sciences. 2000;**11**:235-272

[53] Savastano G, Komjathy A, Shume E, Vergados P, Ravanelli M, Verkhoglyadova O, et al. Advantages of geostationary satellites for ionospheric anomaly studies: Ionospheric plasma depletion following a rocket launch. Remote Sensing. 2019;**11**(14):1734

[54] Bishop G, Walsh D, Daly P, Mazzella A, Holland E. Analysis of the temporal stability of GPS and GLONASS group delay correction terms seen in various sets of ionospheric delay data. In: Proceedings of the 7th International Technical Meeting of the Satellite Division of the Institute of Navigation (ION GPS 1994). 1994. pp. 1653-1661

[55] Demyanov VV, Yasyukevich YV, Jin S, et al. The second-order derivative of gps carrier phase as a promising means for ionospheric scintillation research. Pure and Applied Geophysics. 2019;**176**(10):4555-4573

[56] Savastano G. New applications and challenges of GNSS variometric approach [Ph.D. dissertation]. Rome, Italy: Dept. DICEA, Univ. La Sapienza; 2018

[57] Wei Y et al. Real-time experimental forecast of the Peruvian tsunami of august 2007 for U.S. coastlines. Geophysical Research Letters. 2008;**35**: L04609

[58] Wei Y, Chamberlin C, Titov V, Tang L, Bernard EN. Modeling of the 2011 Japan tsunami - lessons for near-field forecast. Pure and Applied Geophysics. 2013;**170**(6–8):1309-1331

[59] Torrence C, Compo GP. A practical guide to wavelet analysis. Bulletin of the American Meteorological Society. 1998; **79**:6178

[60] Misiti M, Misiti Y, Oppenheim G, Poggi J-M. Wavelet Toolbox. Vol. 15. Natick, MA: The MathWorks Inc.; 1996. p. 21

[61] Klobuchar JA. Ionospheric time-delay algorithm for single-frequency GPS users. IEEE Transactions on Aerospace and Electronic Systems. 1987; **AES-23**(3):325-331

[62] Murray JR, Bartlow N, Bock Y, Brooks BA, Foster J, Freymueller J, et al. Regional global navigation satellite system networks for crustal deformation monitoring. Seismological Research Letters. 2019